Chemical Geology 550 (2020) 119741

Contents lists available at ScienceDirect

Chemical Geology

journal homepage: www.elsevier.com/locate/chemgeo

The isotopic (He, Ne, Sr, Nd, Hf, Pb) signature in the Indian Mantle over 8.8 Ma

Marine Paquet[a,*], Cédric Hamelin[b], Manuel Moreira[a], Mathilde Cannat[a]

[a] Institut de Physique du Globe de Paris, Sorbonne Paris Cité, Université Paris Diderot, UMR7154 CNRS, 1, rue Jussieu, 75238 Paris cedex 05, France
[b] Department of Earth Sciences, University of Bergen, Allegaten 41, 5007 Bergen, Norway

ARTICLE INFO

Editor: Catherine Chauvel

Keywords:
Mid-Ocean Ridge Basalts
Mantle heterogeneity
Noble gases
Isotope geochemistry
Melt/mantle interactions

ABSTRACT

The eastern Southwest Indian Ridge, between 61° and 67°E, has a very low melt supply and comprises several corridors of nearly amagmatic spreading that expose mantle-derived serpentinized peridotite. More volcanically active ridge portions separate these corridors. He, Ne, Pb, Nd, Hf and Sr isotopes were analyzed in basalt glasses dredged on two types of seafloor: volcanic and ultramafic. Basalts dredged on on-axis ultramafic seafloor tend to be slightly more depleted for heavy radiogenic isotopes and show slightly higher $^{3}He/^{4}He$ isotope ratios than basalts dredged on volcanic seafloor, with no systematic difference in neon isotope ratios. We propose that both types of basalts are derived from the same mantle source, but that the basalts dredged on ultramafic seafloor are more affected by melt/mantle reactions, which slightly modify their isotopic signatures. Our dataset also includes a few basalts, dredged on off-axis ultramafic seafloor, that range in age between 2.6 and 8.8 Ma. These few and widely-spaced off-axis samples, erupted at the ridge axis, are a rare opportunity to capture the potential geochemical variability of the mantle source in an ultramafic seafloor corridor over 8.8 Ma. This temporal variability appears to be minor compared to the overall range of isotopic variability of the on-axis lavas from the 61°-67°E region.

1. Introduction

Noble gases (He, Ne) and heavy radiogenic isotopes (Sr, Nd, Hf, Pb) have commonly been used to investigate the nature and the origin of mantle heterogeneities and their time-evolution (Allègre, 1987; Hart, 1988; Hofmann, 1997; Moreira and Allègre, 1998; Sarda et al., 1988, 2000). In particular, it is well established that the Indian Ocean defines a large mantle isotopic domain, different from the mantle of the North Atlantic and the Pacific (e.g. Dupré and Allègre, 1983; Hart, 1984; Hamelin and Allègre, 1985; Hamelin et al., 1986; Mahoney et al., 1989, 1992, 2002; Escrig et al., 2004; Meyzen et al., 2005, 2007). Indian MORBs (Mid Ocean Ridge Basalts) have higher $^{207}Pb/^{204}Pb$, $^{208}Pb/^{204}Pb$ and $^{87}Sr/^{86}Sr$ at a given $^{206}Pb/^{204}Pb$ (Dupré and Allègre, 1983; Hart, 1984). This so-called DUPAL component also tends to have higher $^{4}He/^{3}He$ ratios than the Atlantic or the Pacific (Mahoney et al., 1989; Sarda et al., 2000; Georgen et al., 2003; Raquin and Moreira, 2009; Parai et al., 2012; Gautheron et al., 2015). These geochemical characteristics have been attributed to the injection in the Indian upper mantle of subcontinental lithospheric mantle (e.g. Mahoney et al., 1992), delaminated lower continental crust (e.g. Escrig et al., 2004) or altered oceanic crust and/or sediments (e.g. Dupré and Allègre, 1983; Hart, 1984). These studies only investigated the large-scale variability of the mantle source, using on-axis basaltic samples.

The present study focuses on the easternmost part of the Southwest Indian Ridge (SWIR), between 61° and 67°E (spreading rate ~14 mm.yr^{-1}; Patriat and Segoufin, 1988; Patriat et al., 2008). We use basalt samples collected in this region to investigate the space and time isotopic variability of the mantle source (along and across the ridge axis). This region of the SWIR is an end-member of the global ridge system in terms of low magma supply, which is supported by the seismic crustal structure (Muller et al., 1999), and by gravity data (Cannat et al., 1999, 2006). Underway geophysics, seafloor imagery and dredging (Sauter et al., 2013; Cannat et al., 2003, 2006, 2019) in the 61°-67°E region show that the modes of seafloor spreading are variable along-axis. We distinguish large volcanic centers, where most of the low melt influx to the ridge axis is focused, and corridors of essentially amagmatic spreading (Cannat et al., 2006; Sauter et al., 2013). In these corridors, the seafloor exposes wide expanses of partially serpentinized mantle-derived peridotites, with rare gabbroic intrusive rocks and a thin and discontinuous basaltic cover. Off-axis dredging shows that exhumed serpentinized peridotites have been dominating the landscape in these corridors over the past 8 to 10 Ma. In

* Corresponding author at: Scripps Institution of Oceanography, La Jolla, CA 92093-0244, USA.
E-mail address: mpaquet@ucsd.edu (M. Paquet).

https://doi.org/10.1016/j.chemgeo.2020.119741
Received 19 December 2019; Received in revised form 3 May 2020; Accepted 8 June 2020
Available online 11 June 2020

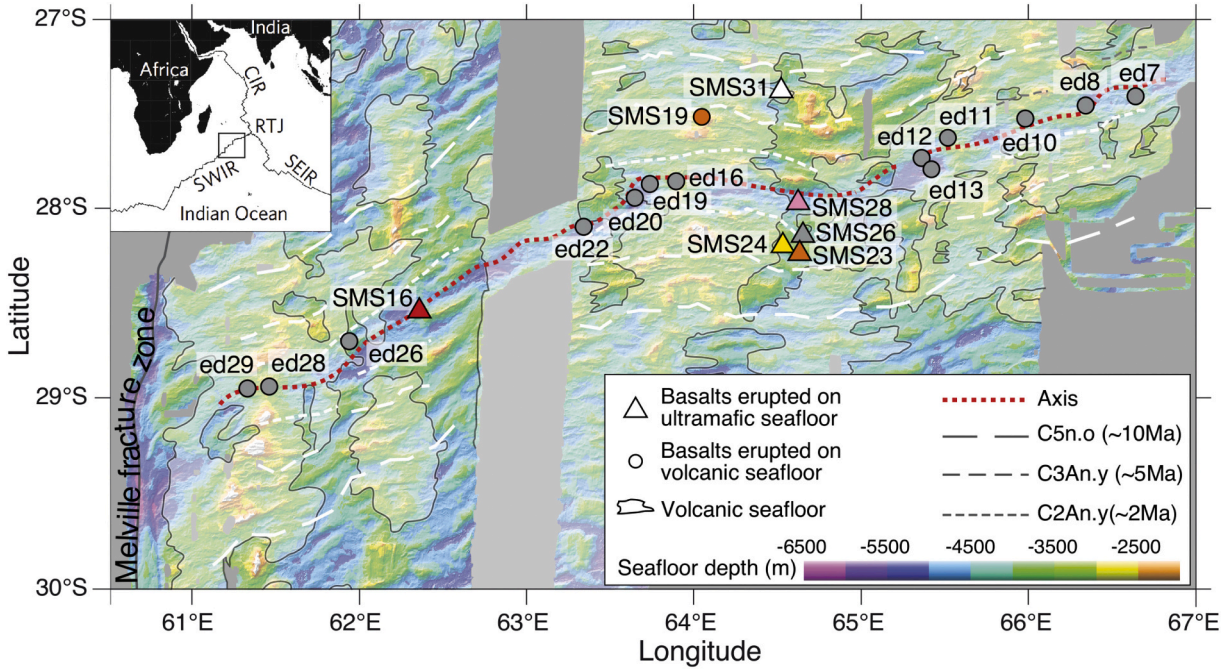

Fig. 1. Location of the dredged samples considered in this study on a bathymetric map of the 61° to 67°E region of the Southwest Indian Ridge (east of the Melville FZ) (after Paquet et al., 2016). SMS6 to SMS35 are dredges from the Smoothseafloor cruise (Sauter et al., 2013); ed7 to ed29 are dredges from the EDUL cruise (Mével et al., 1997). The outlines of the volcanic seafloor domains are from Cannat et al. (2006). (For interpretation of the references to colour in this figure legend, the reader is referred to the web version of this article.)

these regions, seafloor spreading is accommodated by successive large offset normal faults that persist for 1 to 3 Ma and dip alternatively to the north beneath the African-Somalian plate, or to the south beneath the Antarctic plate (Sauter et al., 2013). The two types of seafloor (volcanic and nearly-amagmatic) exposed in the 61°-67°E SWIR region have been dredged during the EDUL (Meyzen et al., 2003; Seyler et al., 2003), and Smoothseafloor (Sauter et al., 2013; Paquet et al., 2016) cruises. This study is based on samples from both cruises (Fig. 1): basalts dredged from the sparse volcanic cover of the nearly amagmatic corridors ("basalts dredged or erupted on ultramafic seafloor"), and basalts dredged on volcanic seafloor, both sampled on- and off-axis.

Major, trace element compositions for the on-axis samples, and Pb and Nd isotopic data for a subset of on-axis basalts dredged on ultramafic and volcanic seafloors have been published in Paquet et al. (2016). On-axis basalts erupted on ultramafic seafloor in this subset show isotopic compositions consistent with those of the basalts erupted at the volcanic centers, also Published by Meyzen et al. (2005). The authors also reported that basalts erupted on ultramafic seafloor tend to have lower $^{206}Pb/^{204}Pb$ ratios than those from the volcanic seafloor, but that this difference is not visible with the other Pb isotopic ratios, or with Nd. In the present study, we analyze additional samples, including basalts dredged off-axis from both types of seafloor, and we provide data on other isotopic systems: Sr, Hf, He and Ne. We address the following questions: What is the isotopic variability of the mantle at present day along the ridge axis? What are the effects of melt/mantle reactions on the isotopic compositions of the two types of basalts? Is the mantle isotopic signature homogeneous over time in this region of the SWIR?

2. Analytical methods

2.1. Sr, Nd, Hf and Pb isotopes

For samples with fresh glass, glass chips were handpicked and washed for 10 min in 1% H_2O_2 in an ultrasonic bath, followed by three rinses in ultrapure water and then leached briefly in concentrated ultrapure HBr prior to digestion in concentrated HBr-HF ultrapure acids (1:3). For the samples without fresh glass, cores of the pillows were separated, crushed and finely powdered. Powders were leached in 6 M HCl at 130 °C for 1 h, followed by three rinses in ultrapure water and drying, prior to digestion (e.g. Baker et al., 2004; Hamelin et al., 2009, 2013). Lead was extracted after the method of Hamelin et al. (2013), modified from Manhes et al. (1978). Sr, Nd and Hf separation was completed using a method adapted from Hamelin et al. (2013).

Nd and Pb isotopic compositions were measured at the Institut de Physique du Globe de Paris using a ThermoFinnigan Neptune. Sr and Hf isotopic compositions were measured at the Bergen Analytical Facility, using a TIMS MAT 262 and a ThermoFinnigan Neptune respectively. All Nd data were corrected for mass fractionation using $^{146}Nd/^{144}Nd = 0.7219$. Repeated measurements of NIST3135A and JNdi standards during analyses gave an average of $^{143}Nd/^{144}Nd = 0.511367 \pm 5$ ($n = 22$, 2σ) and $^{143}Nd/^{144}Nd = 0.512110 \pm 3$ ($n = 8$, 2σ) respectively. Mass fractionation on Pb was monitored using a thallium doping and sample-standard bracketing technique (Rehkämper and Mezger, 2000; White et al., 2000; Meyzen et al., 2005). Data are reported relative to published values of NBS 981 (Catanzaro et al., 1968). 17 replicates of the Pb isotope standard NIST981 gave an average of 17.062 ± 0.002 (2σ) and 15.663 ± 0.002 (2σ) and 37.243 ± 0.007 (2σ) for $^{206}Pb/^{204}Pb$, $^{207}Pb/^{204}Pb$ and $^{208}Pb/^{204}Pb$ respectively. The estimated external precision for Pb analyses is ± 0.01%, 2σ for $^{206}Pb/^{204}Pb$ and $^{207}Pb/^{204}Pb$ and ± 0.02%, 2σ for $^{208}Pb/^{204}Pb$. Analytical blanks were lower than 40 pg for Nd and 30 pg for Pb. 7 replicates of the Sr isotope standard SRM987 gave an average of 0.710239 ± 10 (2σ). Repeated measurements of JMC475 standards during analyses gave an average of $^{176}Hf/^{177}Hf = 0.282148 \pm 1$ (n = 22, 2σ).

2.2. Helium and neon isotopes

Noble gases were measured at the Institut de Physique du Globe de Paris using the Multi-Collection Noble Gas Mass Spectrometer Noblesse from Nu instruments ©. Glass chips were cleaned using peroxide in an ultrasonic bath, or oxalic acid on a hot plate at 80 °C, depending on the sample alteration. Samples were baked overnight at 150 °C under

Table 1
Hf, Nd, Sr, Pb isotopic compositions for volcanic and ultramafic seafloor basalts from the 61°-67°E region of the Southwest Indian Ridge.

Sample	Latitude (°)	Longitude (°)	Depth (m)	Age (Ma)	Seafloor	$^{176}Hf/^{177}Hf$	2σ	ε_{Hf}	$^{143}Nd/^{144}Nd$	2σ	ε_{Nd}	$^{87}Sr/^{86}Sr$	2σ	$^{206}Pb/^{204}$-Pb	2σ	$^{207}Pb/^{204}$-Pb	2σ	$^{208}Pb/^{204}$-Pb	2σ
ED-DR8-1-2	−27.35	66.34	4550	<0.78	Volcanic	0.283189	0.000007	14.75	0.513039	0.000005	7.82	0.702970	0.000008	17.7804	0.0005	15.4504	0.0004	37.7122	0.0011
ED-DR9-2-3	−27.43	66.26	4500	<0.78	Volcanic	0.283161	0.000005	13.77	0.513010	0.000005	7.26	0.703067	0.000008	17.9202	0.0006	15.4646	0.0005	37.8545	0.0013
ED-DR10-3-16	−27.57	65.98	4320	<0.78	Volcanic	0.283190	0.000004	14.78	0.513044	0.000005	7.93	0.702921	0.000008	17.7960	0.0005	15.4506	0.0005	37.7020	0.0012
ED-DR11-2-7	−27.62	65.53	3550	<0.78	Volcanic	0.283104	0.000005	11.75	0.512918	0.000005	5.47	0.703441	0.000009	18.0021	0.0006	15.4916	0.0005	38.0784	0.0012
ED-DR12-2-2	−27.74	65.35	5550	<0.78	Volcanic	0.283187	0.000004	14.69	0.513049	0.000004	8.03	0.702930	0.000008	17.8860	0.0005	15.4582	0.0004	37.8148	0.0011
ED-DR12-3-1	−27.74	65.35	5550	<0.78	Volcanic	0.283174	0.000011	14.22	0.513055	0.000004	8.13	0.702921	0.000008	17.8861	0.0005	15.4568	0.0005	37.8132	0.0012
ED-DR12-3-2	−27.74	65.35	5550	<0.78	Volcanic	0.283175	0.000004	14.26	0.513054	0.000004	8.12	0.702917	0.000008	17.8864	0.0004	15.4567	0.0004	37.8130	0.0009
ED-DR13-3-2	−27.78	65.41	5450	<0.78	Volcanic	0.283173	0.000003	14.17	0.513033	0.000005	7.71	0.703059	0.000009	17.8124	0.0006	15.4550	0.0006	37.7632	0.0014
ED-DR16-1-1	−27.85	63.91	2800	<0.78	Volcanic	0.283181	0.000006	14.47	0.513077	0.000004	8.56	0.703403	0.000008	17.8042	0.0005	15.4407	0.0004	37.6538	0.0009
ED-DR16-3-1	−27.85	63.91	2800	<0.78	Volcanic	0.283183	0.000003	14.54	0.513079	0.000004	8.60	0.702774	0.000008	17.8158	0.0005	15.4415	0.0004	37.6754	0.0011
ED-DR22-2-1	−28.11	63.36	4950	<0.78	volcanic	0.283190	0.000004	14.79	0.513110	0.000005	9.21	0.702684	0.000008	17.8987	0.0006	15.4559	0.0006	37.7308	0.0014
ED-DR26-1-2	−28.80	61.93	4600	<0.78	Volcanic	0.283172	0.000006	14.15	0.513053	0.000005	8.09	0.703831	0.000008	17.9605	0.0066	15.4683	0.0056	37.8395	0.0142
SMS-DR16-3-4	−28.54	62.36	3850	<0.78	Ultramafic				0.513098	0.000004	8.98	0.702906	0.000008	17.7693	0.0009	15.4439	0.0007	37.5873	0.0020
SMS-DR16-3-5	−28.54	62.36	3850	<0.78	Ultramafic				0.513093	0.000004	8.87	0.702786	0.000008	17.7560	0.0011	15.4380	0.0006	37.4953	0.0017
SMS-DR16-3-7	−28.54	62.36	3850	<0.78	Ultramafic				0.513082	0.000005	8.67	0.702931	0.000008	17.7895	0.0010	15.4503	0.0009	37.5191	0.0025
SMS-DR16-3-9	−28.54	62.36	3850	<0.78	Ultramafic				0.513087	0.000004	8.76	0.702866	0.000008	17.7579	0.0009	15.4423	0.0009	37.5327	0.0022
SMS-DR16-3-14	−28.54	62.36	3850	<0.78	Ultramafic				0.513098	0.000004	8.97	0.702703	0.000008	17.7624	0.0007	15.4389	0.0006	37.5764	0.0014
SMS-DR19-4-4	−27.51	64.06	2650	5.30	Volcanic	0.283208	0.000005	15.42	0.513085	0.000004	8.72	0.703211	0.000008	17.7694	0.0008	15.4332	0.0006	37.6240	0.0018
SMS-DR23-2-2	−28.23	64.63	3870	4.90	Ultramafic	0.283199	0.000006	15.10	0.513076	0.000004	8.55	0.703755	0.000008	17.7910	0.0005	15.4443	0.0004	37.6590	0.0012
SMS-DR23-2-10	−28.23	64.63	3870	4.90	Ultramafic	0.283197	0.000004	15.04	0.513078	0.000004	8.58	0.702782	0.000009	17.7908	0.0006	15.4418	0.0006	37.6564	0.0010
SMS-DR23-2-11	−28.23	64.63	3870	4.90	Ultramafic	0.283198	0.000005	15.06	0.513076	0.000004	8.55	0.703402	0.000007	17.8130	0.0008	15.4445	0.0006	37.6888	0.0017
SMS-DR24-2-3	−28.19	64.54	3830	3.80	Ultramafic	0.283176	0.000006	14.30	0.513033	0.000004	7.70	0.703651	0.000008	17.8786	0.0003	15.4654	0.0003	37.8237	0.0006
SMS-DR24-2-6	−28.19	64.54	3830	3.80	Ultramafic				0.513010	0.000005	7.26	0.703441	0.000008	17.8780	0.0004	15.4648	0.0005	37.6740	0.0007
SMS-DR26-3-1	−28.15	64.65	3960	2.60	Ultramafic	0.283186	0.000005	14.65	0.513052	0.000004	8.08	0.703048	0.000009	17.8455	0.0003	15.4515	0.0003	37.7467	0.0006
SMS-DR26-3-2	−28.15	64.65	3960	2.60	Ultramafic	0.283190	0.000006	14.80	0.513058	0.000004	8.19	0.703561	0.000009	17.8417	0.0005	15.4515	0.0005	37.7427	0.0011
SMS-DR28-3-3	−27.96	64.63	4550	<0.78	Ultramafic	0.283197	0.000005	15.03	0.513078	0.000004	8.59	0.703033	0.000009	17.6898	0.0004	15.4407	0.0003	37.5480	0.0010

Table 2
He and Ne results obtained on the Noblesse Mass Spectrometer for volcanic and ultramafic seafloor basalts from the 61°-67°E region of the Southwest Indian Ridge. Concentrations are in ccSTP/g.

Sample	Age	Seafloor	Weight (g)	R/R_a	±1σ	$^4He/^3He$	±1σ	^4He (x10^{-6})	^{22}Ne (x10^{-12})	$^{20}Ne/^{22}Ne$	±1σ	$^{21}Ne/^{22}Ne$	±1σ	^3He (x10^{-12})	$^3He/^{22}Ne$
ED-DR7-2-8 NJ	<0.78	Volcanic	0.010	7.77	0.07	92,957	792	37.2							
ED-DR8-1-2	<0.78	Volcanic	0.143	7.49	0.05	96,355	635	48.2	37.0	11.87	0.08	0.0534	0.0010	500.5	13.514
ED-DR9-2-3	<0.78	Volcanic	0.096	7.72	0.06	93,521	686	23.3	18.1	11.43	0.05	0.0483	0.0005	249.2	13.780
ED-DR10-3-16	<0.78	Volcanic	0.092	7.89	0.06	91,531	695	2.4	12.8	10.56	0.04	0.0338	0.0005	26.5	2.076
ED-DR11-1-9	<0.78	Volcanic	0.010	7.61	0.06	94,869	810	40.8						429.6	
ED-DR11-2-7	<0.78	Volcanic	0.130	7.49	0.05	96,351	682	6.8	338.9	9.93	0.04	0.0303	0.0004	70.6	0.208
ED-DR11-2-10	<0.78	Volcanic	0.044					4.6	18.8	10.70	0.06	0.0386	0.0008		
ED-DR12-2-2	<0.78	Volcanic	0.065	7.82	0.05	92,307	557	1.4	43.4	9.84	0.04	0.0293	0.0004	15.6	0.358
ED-DR12-3-1	<0.78	Volcanic	0.067	7.59	0.06	95,067	744	2.6	2.5	10.26	0.39	0.0364	0.0022	27.2	10.651
ED-DR12-3-2	<0.78	Volcanic	0.136	7.78	0.07	92,842	839	2.0	22.9	9.94	0.03	0.0299	0.0006	21.1	0.919
ED-DR13-3-2	<0.78	Volcanic	0.055	7.98	0.14	90,495	1632	0.1						1.4	
ED-DR16-1-1	<0.78	Volcanic	0.156	7.57	0.05	95,400	651	60.4	171.8	10.04	0.04	0.0321	0.0004	633.4	3.686
ED-DR16-2-1	<0.78	Volcanic	0.010	7.55	0.11	95,567	1404	0.8	632.7	9.86	0.04	0.0297	0.0004	8.1	0.013
ED-DR16-2-3	<0.78	Volcanic	0.009	7.48	0.04	96,587	485	36.9	23.6	12.22	0.22	0.0551	0.0025	382.1	16.193
ED-DR16-3-1	<0.78	Volcanic	0.048	7.28	0.05	99,193	625	42.1	16.2	11.82	0.09	0.0545	0.0015	424.2	26.166
ED-DR19-1-3	<0.78	Volcanic	0.232	7.61	0.05	94,901	626	32.9	311.7	10.10	0.06	0.0309	0.0002	346.9	1.113
ED-DR22-2-1	<0.78	Volcanic	0.194	7.91	0.05	91,265	618	1.5	1.1	12.30	0.18	0.0604	0.0028	16.8	15.966
ED-DR26 type1	<0.78	Volcanic	0.074	8.16	0.09	88,507	1030	0.2						1.8	
ED-DR26-1-2	<0.78	Volcanic	0.098	8.12	0.06	88,950	693	1.7						19.5	
ED-DR28-2-5	<0.78	Volcanic	0.100	7.76	0.04	93,026	485	7.7	8.3	10.73	0.06	0.0422	0.0009	82.7	9.966
ED-DR29-1-1	<0.78	Volcanic	0.077	7.19	0.03	100,479	488	15.6	18.4	10.35	0.06	0.0385	0.0008	155.0	8.419
ED-DR29-1-2	<0.78	Volcanic	0.060	6.91	0.03	104,415	505	24.7	18.3	11.57	0.06	0.0509	0.0009	236.4	12.943
SMS-DR16-3-4	<0.78	Ultramafic	0.020	8.02	0.07	90,063	771	15.1						167.4	
SMS-DR16-3-5	<0.78	Ultramafic	0.021	7.99	0.06	90,329	672	21.7	46.1	10.61	0.05	0.0369	0.0007	240.7	5.222
SMS-DR16-3-7	<0.78	Ultramafic	0.237	6.83	0.04	105,677	625	31.3	86.6	11.30	0.05	0.0484	0.0008	296.3	3.424
SMS-DR16-3-9	<0.78	Ultramafic	0.021	8.11	0.07	88,994	722	6.6	16.0	10.98	0.09	0.0389	0.0017	74.2	4.622
SMS-DR16-3-14	<0.78	Ultramafic	0.019	7.73	0.07	93,447	799	20.6						220.0	
SMS-DR19-4-1	5.30	Volcanic	0.086	4.22	0.18	171,288	7210	0.02	130.7	9.89	0.04	0.0304	0.0003		
SMS-DR19-4-4	5.30	Volcanic	0.188	8.06	0.06	89,626	704	0.8	11.9	11.58	0.04	0.0497	0.0007	9.3	0.783
SMS-DR23-2-2	4.90	Ultramafic	0.466	8.02	0.06	90,028	683	3.6	9.4	11.09	0.04	0.0442	0.0006	40.2	4.289
SMS-DR23-2-10	4.90	Ultramafic	0.023	8.04	0.08	89,855	854	2.9						32.4	
SMS-DR23-2-11	4.90	Ultramafic	0.167	7.95	0.08	90,855	863	0.4	49.3	9.96	0.04	0.0306	0.0005	4.5	0.090
SMS-DR24-2-3	3.80	Ultramafic	0.054	7.69	0.15	93,841	1789	0.1						0.8	
SMS-DR24-2-6	3.80	Ultramafic	0.109	7.98	0.09	90,508	974	0.2	2.7	12.20	0.10	0.0533	0.0016	2.6	0.950
SMS-DR26-3-1	2.60	Ultramafic	0.546	5.47	0.40	131,969	9649	0.02	4.8	10.14	0.04	0.0315	0.0004		
SMS-DR26-3-2	2.60	Ultramafic	0.123	7.72	0.17	93,546	2110	0.02						0.3	
SMS-DR28-3-3	<0.78	Ultramafic	0.046	7.86	0.07	91,904	807	1.7	1.9					18.5	9.881
SMS-DR31-2-4	8.80	Ultramafic	0.248	7.57	0.31	95,357	3965	0.02						0.2	

Table 3
Model parameters used in Fig. 7.

	Pb (ppb)	$^{206}Pb/^{204}Pb$	$^{208}Pb/^{204}Pb$
DMM	44.0	16.5	35.7
Enriched component	680.0	18.04	38.13

DMM values are from Meyzen et al. (2005).

vacuum then crushed under vacuum and purified with a titanium getter heated at 800 °C for 5 min. The getter was then turned off in order to decrease its temperature at room temperature to trap hydrogen. After 10 min, noble gases were adsorbed on charcoal at 10 K using a cryogenic trap. Helium was separated from neon at 35 K before being introduced in the mass spectrometer. Neon was desorbed at 70 K and then analyzed using the technique of Moreira et al. (2011).

3. Sampling and data processing

38 basaltic glass samples from 20 dredges (locations shown in Fig. 1) were analyzed in this study. Most samples are aphyric, with variable amounts of vesicles. 14 samples come from 6 dredges in nearly-amagmatic corridors, including 8 off-axis samples from 4 dredges. The other 24 samples come from 14 dredges in volcanic domains, including 2 off-axis samples from a single dredge. Radiogenic and noble gas isotope compositions of some of these volcanic seafloor basalts were analyzed in the earlier work of Meyzen et al. (2003, 2005), and Gautheron et al. (2015). New isotope data were acquired for 26 samples (12 from the EDUL cruise, and 14 from the Smoothseafloor cruise), and noble gases data for 38 samples (22 from the EDUL cruise, and 16 from the Smoothseafloor cruise).

In this study, off-axis samples are thought to be erupted at the ridge axis and are now off-axis due to seafloor spreading. The age of the off-axis samples is estimated using the distance to the closest magnetic anomaly and a constant spreading rate of 14 mm.yr^{-1}, based on magnetic anomalies (Patriat and Segoufin, 1988; Cannat et al., 2006). Sr, Nd, Hf and Pb isotope ratios for off-axis samples have been corrected from radioactive decay with their estimated age and recalculated to obtain the isotopic ratios at the time of the eruption at the ridge axis. Because the off-axis samples are no older than 8.8 Ma, the radioactive decay correction induces changes that are lower than the uncertainties

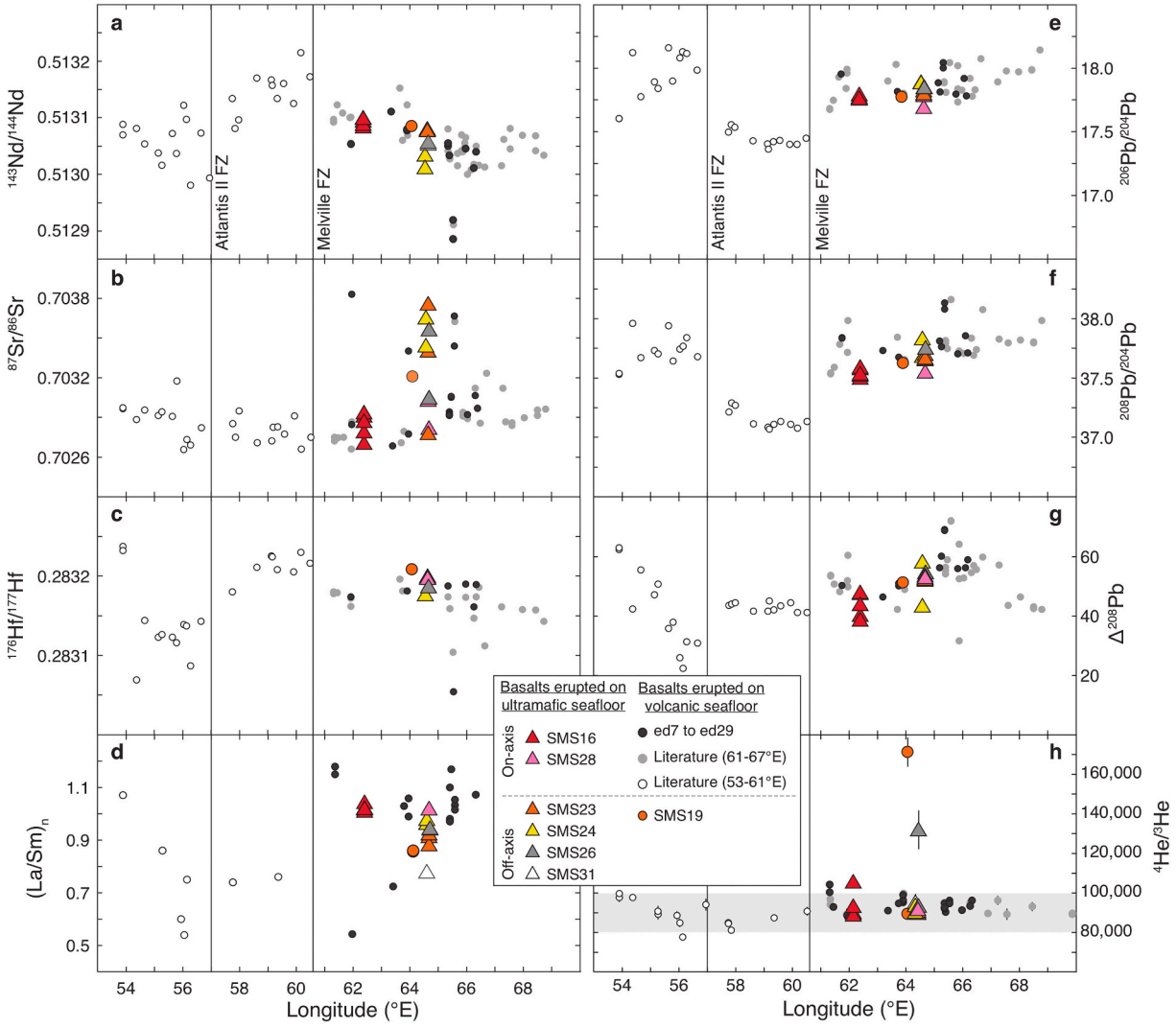

Fig. 2. (a) $^{143}Nd/^{144}Nd$, (b) $^{87}Sr/^{86}Sr$, (c) $^{176}Hf/^{177}Hf$, (d) $(La/Sm)_n$, (e) $^{206}Pb/^{204}Pb$, (f) $^{208}Pb/^{204}Pb$, (g) $\Delta^{208}Pb$, (h) $^{4}He/^{3}He$ in function of longitude along the Southwest Indian Ridge, between 53° and 70°E. Triangles represent basalts collected in ultramafic seafloor areas of the 61°-67°E SWIR region (colored by dredge number as in Fig. 1), and dark grey circles correspond to basalts collected in volcanic seafloor areas. The open circles and light grey circles are basalts collected between 53° and 61°E, and between 61° and 67°E of the Southwest Indian Ridge respectively (Meyzen et al., 2003, 2005, 2007), except for $^{4}He/^{3}He$ data, which are from Mahoney et al. (1989) and Gautheron et al. (2015). The grey area in (h) corresponds to the mean MORB value of 90,000 ± 10,000 (Allègre et al., 1995). (For interpretation of the references to colour in this figure legend, the reader is referred to the web version of this article.)

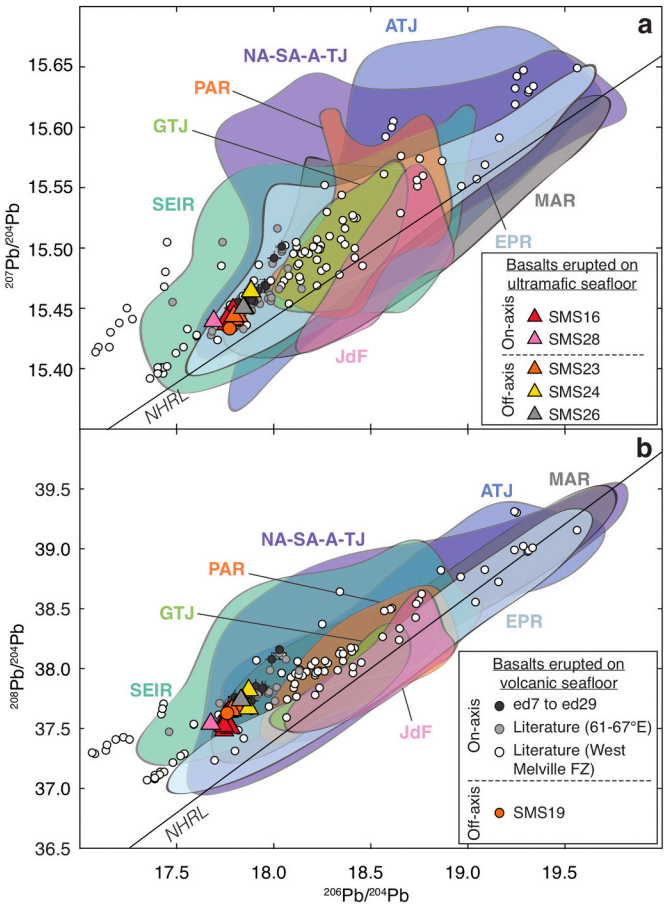

Fig. 3. (a) $^{207}Pb/^{204}Pb$, (b) $^{208}Pb/^{204}Pb$ in function of $^{206}Pb/^{204}Pb$. Triangles represent basalts collected in ultramafic seafloor areas of the 61°-67°E SWIR region (colored by dredge number as in Fig. 1), and dark grey circles correspond to basalts collected in volcanic seafloor areas. The light grey and open circles are basalts collected between 61° and 67°E, and West of the Melville Fracture Zone along the Southwest Indian Ridge respectively (Hamelin and Allègre, 1985; Mahoney et al., 1989, 1992; Le Roex et al., 1989; Meyzen et al., 2005). All the colored fields correspond to PetDB (www.earthchem.org/petdb, Lehnert et al., 2000) data for the Mid-Atlantic Ridge (MAR), East Pacific Rise (EPR), Azores Triple Junction (ATJ), North America-South America-Africa Triple Junction (NA-SA-A-TJ), Southeast Indian Ridge (SEIR), Pacific-Antartic Ridge (PAC), Galapagos Triple Junction (GTJ), and Juan de Fuca and Gorda Ridge (JdF). (For interpretation of the references to colour in this figure legend, the reader is referred to the web version of this article.)

for Sr, Nd and Hf. For Pb isotopic ratios, the correction leads to changes up to 0.005, which is on the same order of magnitude than the uncertainties. For $^{4}He/^{3}He$ ratios, because we analyzed gases from the vesicles by crushing and because U and Th are not present in these vesicles, no correction for radiogenic ^{4}He is needed. All the data, including the radioactive-decay-corrected isotopic ratios are presented in Tables 1 and 2 (see Table S1 for the compilation of major, trace and isotope data for all the samples from the 61–67°E region).

4. Results

4.1. Sr, Nd, Hf and Pb isotopes

Basalts erupted on volcanic seafloor range from 17.8 to 18.0 for $^{206}Pb/^{204}Pb$, from 15.4 to 15.5 for $^{207}Pb/^{204}Pb$, from 37.6 to 38.1 for $^{208}Pb/^{204}Pb$, from 0.512885 to 0.513110 for $^{143}Nd/^{144}Nd$, from 0.283014 to 0.283208 for $^{176}Hf/^{177}Hf$, and from 0.702684 to 0.703831 for $^{87}Sr/^{86}Sr$. Basalts erupted on ultramafic seafloor range from 17.7 to 17.9 for $^{206}Pb/^{204}Pb$, from 15.4 to 15.5 for $^{207}Pb/^{204}Pb$, from 37.5 to 37.8 for $^{208}Pb/^{204}Pb$, from 0.513010 to 0.513098 for $^{143}Nd/^{144}Nd$, from 0.283176 to 0.283199 for $^{176}Hf/^{177}Hf$, and from 0.702703 to 0.703755 for $^{87}Sr/^{86}Sr$. These compositions are similar to those reported by Meyzen et al. (2005) for volcanic seafloor basalts (Figs. 2, 3 and 4). Basalt samples from the 61°-67°E region are characterized by higher $^{207}Pb/^{204}Pb$ and $^{208}Pb/^{204}Pb$ at a given $^{206}Pb/^{204}Pb$ than their Atlantic and Pacific counterparts (Fig. 3), which is coherent with the Indian Ocean MORB characteristics (e.g. Dupré and Allègre, 1983; Hart, 1984; Hamelin and Allègre, 1985; Hamelin et al., 1986; Mahoney et al., 1989, 1992, 2002; Escrig et al., 2004; Meyzen et al., 2005, 2007; Hanan et al., 2013). All isotopic ratios measured in the basalts from the 61° to 67°E region of the SWIR are in agreement with the trend defined between 61° and 67°E by Meyzen et al. (2005) (Table 1, Fig. 2a, b, c, e, f, g). Our new data also confirm the existence of an along-axis trend with more radiogenic samples in Pb and Sr isotopes towards the east (at 61°E, $^{208}Pb/^{204}Pb$ = 37.84, $^{206}Pb/^{204}Pb$ = 17.96, $^{87}Sr/^{86}Sr$ = 0.703831; and at 67°E, $^{208}Pb/^{204}Pb$ = 37.71, $^{206}Pb/^{204}Pb$ = 17.78, $^{87}Sr/^{86}Sr$ = 0.702970), and less radiogenic in Nd and Hf isotopes (at 61°E, $^{143}Nd/^{144}Nd$ = 0.513053 and $^{176}Hf/^{177}Hf$ = 0.283172; at 67°E, $^{143}Nd/^{144}Nd$ = 0.513039 and $^{176}Hf/^{177}Hf$ = 0.283189) (Meyzen et al., 2005).

However, only considering the on-axis lavas, basalts erupted on ultramafic seafloor appear less radiogenic than those erupted on volcanic seafloor: they have lower $^{206}Pb/^{204}Pb$, $^{207}Pb/^{204}Pb$, $^{208}Pb/^{204}Pb$ ratios, and higher $^{143}Nd/^{144}Nd$ (and $^{176}Hf/^{177}Hf$) ratios. For each isotopic ratio, we performed a two-sample Kolmogorov-Smirnov test to check that these two populations are compositionally distinct (e.g. Miller and Miller, 2018). We obtain the following D values for $^{206}Pb/^{204}Pb$, $^{207}Pb/^{204}Pb$, $^{208}Pb/^{204}Pb$ and $^{143}Nd/^{144}Nd$ respectively: 0.92, 0.85, 1.0 and 0.85, where D is the maximum absolute value of the difference between the cumulative distribution functions for the on-axis basalts from both types of seafloor. For a confidence level of $\alpha = 0.05$, the D values need to be greater than $D_{criteria} = \sqrt{-ln(\alpha/2)/2} \times \sqrt{(n_1 + n_2)/n_1/n_2} = 0.67$, where n_1 and n_2 are the numbers of samples in each population. We conclude that the compositional differences observed between on-axis basalts erupted on ultramafic and volcanic seafloors are statistically significative (see Table S2 for details).

Off-axis samples display a larger range of $^{87}Sr/^{86}Sr$ values (between 0.702782 and 0.703755; Fig. 2c) and plot out of the global MORB trend in the ε_{Hf} versus $^{87}Sr/^{86}Sr$ diagram (Fig. 4b). This large isotopic variability is not visible for the other isotopic ratios (Figs. 2a, b, e, f, g and 4a). Multiple isotopic compositions measured in basalt samples from a single dredge are homogeneous in most cases.

One dredge (ED-DR11 at 65.53°E) shows lower $^{143}Nd/^{144}Nd$ and $^{176}Hf/^{177}Hf$, and higher $^{87}Sr/^{86}Sr$, $^{206}Pb/^{204}Pb$, $^{207}Pb/^{204}Pb$, $^{208}Pb/^{204}Pb$ and $\Delta^{208}Pb$ (where $\Delta^{208}Pb$ represents the offset of $^{208}Pb/^{204}Pb$ relative to the Northern Hemisphere reference line at a given $^{206}Pb/^{204}Pb$, as defined by Hart, 1984) than the rest of the samples of the 61° to 67°E region, which confirms the results reported by Meyzen et al. (2005) for Pb, Nd and Sr isotope compositions for samples from the same dredge.

4.2. He and Ne isotopes

Most of the samples from the 61° to 67°E region of the SWIR have $^{4}He/^{3}He$ ratios between 88,507 ($^{3}He/^{4}He$ = 8.16 R_a where R_a is the atmospheric ratio) and 105,677 ($^{3}He/^{4}He$ = 6.83 R_a), for an average value of 96,807 ± 14,611, or 7.72 ± 0.32 R_a (Table 2, Fig. 2h), and with ^{4}He contents varying between 0.02 and 60 μccSTP/g (Fig. 5a). Two samples (SMS-DR19-4-1 and SMS-DR26-3-1) have higher $^{4}He/^{3}He$ ratios (131,969–171,288), associated with very low ^{4}He concentrations (~0.02 μccSTP/g). Georgen et al. (2003) calculated that the $^{3}He/^{4}He$ ratio of samples with ^{4}He = 4 μccSTP/g would decrease by 10% over ~10 Ma due to post-eruptive radiogenic ingrowth (assuming

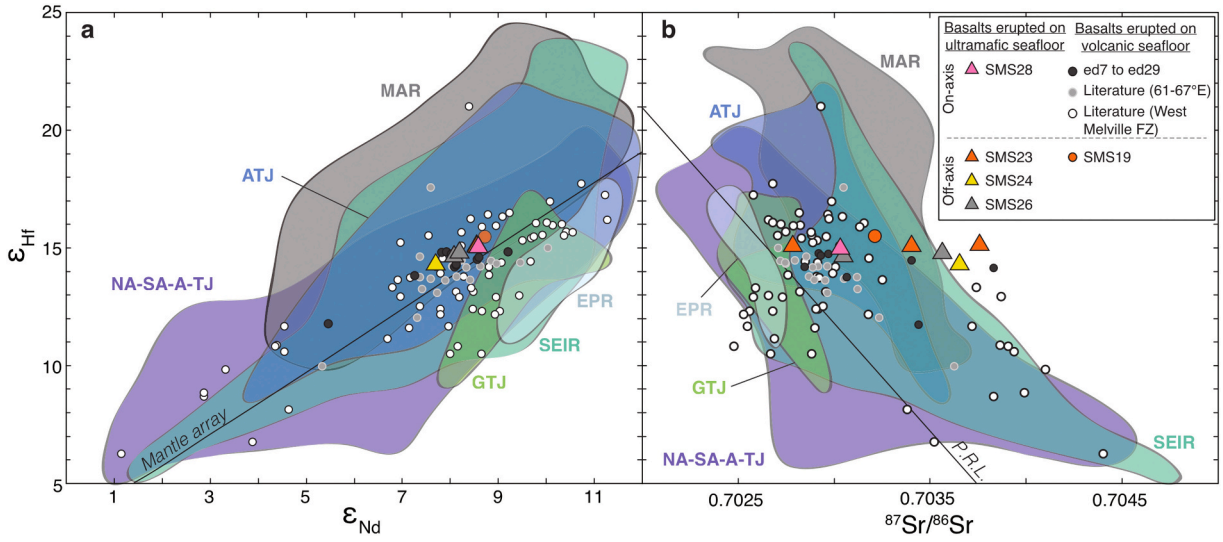

Fig. 4. ε_{Hf} in function of (a) ε_{Nd} and (b) $^{87}Sr/^{86}Sr$. Same symbols as in Figs. 2 and 3. Mantle array and Pacific Reference Line (P.R.L.) from Vervoort et al. (1999) and Vlastelic et al. (1999). Literature data from Hamelin and Allègre, 1985; Mahoney et al., 1989, 1992; le Roex et al., 1989; Chauvel and Blichert-Toft, 2001; Janney et al., 2005; Meyzen et al., 2005. (For interpretation of the references to colour in this figure legend, the reader is referred to the web version of this article.)

[U] = 0.6 ppm, and Th/U = 3). Only $^{3}He/^{4}He$ ratios for samples with ^{4}He above or equal to a cutoff of 0.1 μccSTP/g are considered representative of the mantle ratio, considering a smaller contribution of radiogenic ingrowth for the basalts from the 61°-67°E region due to their lower U content (~0.1 ppm) but similar Th/U. The remaining high-^{4}He samples correspond to typical MORB isotopic ratios (90,000 ± 10,000 or R/Ra = 8 ± 1; Allègre et al., 1995) and are similar to the values reported by Gautheron et al. (2015) for samples of the EDUL cruise (Fig. 2h) in the same region, and also coherent with basalts collected further West along the SWIR (e.g. Mahoney et al., 1989; Georgen et al., 2003; Raquin and Moreira, 2009; Parai et al., 2012; Graham et al., 2014). We note that basalts from segment K along the SEIR show similar $^{3}He/^{4}He$ ratios with an average value of 7.66 ± 0.086 R_a (Graham et al., 2014). The helium isotopic ratios reported in basalt samples from a given dredge are in most cases homogeneous. Basalts dredged on ultramafic seafloor, especially on-axis samples, show slightly lower $^{4}He/^{3}He$ ratios (higher $^{3}He/^{4}He$ ratios) than those collected on the volcanic seafloor (Fig. 5), with overlap between the two groups. We obtain a D value of 0.43 for the two-sample Kolmogorov-Smirnov test for $^{3}He/^{4}He$ for a $D_{criteria}$ of 0.63: the compositional differences observed between on-axis basalts erupted on ultramafic and volcanic seafloors are not statistically significative (Table S2). Moreover, off-axis samples tend to have lower ^{4}He contents (between 0.1 and 3.6 μccSTP/g) than on-axis samples (from 0.1 to 60 μccSTP/g), with no systematic differences in $^{4}He/^{3}He$ ratios (Fig. 5a).

Both types of basalts from the 61° to 67°E region of the SWIR have ^{22}Ne contents between 1.0×10^{-12} and 6.3×10^{-10} ccSTP/g. $^{20}Ne/^{22}Ne$ and $^{21}Ne/^{22}Ne$ ratios range respectively between 9.8 ± 0.04 and 12.3 ± 0.18, and between 0.0293 ± 0.0004 and 0.0604 ± 0.0028 respectively (Table 2, Fig. 5b). The minimum values of these ranges are identical to the atmospheric isotopic ratios ($^{20}Ne/^{22}Ne$ = 9.8 and $^{21}Ne/^{22}Ne$ = 0.029, respectively). All samples fall on the MORB line defined by Sarda et al. (1988) in the three neon isotopes diagram (Fig. 5b). Following Moreira and Allègre (1998), it is possible to correct the $^{21}Ne/^{22}Ne$ ratios for air contamination to obtain the $^{21}Ne/^{22}Ne$ ratio of the magma ($^{21}Ne/^{22}Ne_{mantle}$). This method is valid for samples with raw values of $^{20}Ne/^{22}Ne$ ratios >10.5. For lower $^{20}Ne/^{22}Ne$ values, the isotopic composition is too close to the air composition, and it creates artificial variability and large uncertainties. The MORB source end-member – free of atmospheric contamination – corresponds to the intersection of the MORB line and of the $^{20}Ne/^{22}Ne$ value of the primitive mantle (Moreira and Allègre, 1998), because ^{20}Ne and ^{22}Ne are almost entirely non-radiogenic isotopes. In this study, we use the 12.6 value proposed by Moreira (2013) for the $^{20}Ne/^{22}Ne$ ratio of the uncontaminated mantle. We observe no significant difference in $^{20}Ne/^{22}Ne$ and $^{21}Ne/^{22}Ne$ ratios between basalts erupted on ultramafic and volcanic seafloors, or between on- and off-axis samples: on-axis samples show $^{21}Ne/^{22}Ne_{mantle}$ values between 0.046 and 0.064 and samples dredged off-axis range from 0.056 to 0.060 (Fig. 6a). The $^{21}Ne/^{22}Ne_{mantle}$ corrected for the sample SMS-DR28-3-3, which corresponds to the on-axis basalt of the eastern amagmatic spreading corridor, is not reported in this study due to analytical issues during the data acquisition, which limits the discussion about a possible time-evolution of the neon isotopic signature of the mantle.

5. Discussion

At first glance, our new dataset is showing that all the basalts from the 61°-67°E region of the SWIR, whether they were dredged on- or off-axis, on ultramafic or volcanic seafloor, have similar trace element and Nd, Hf, Pb, He and Ne isotope compositions (Fig. 2), compared to the global variability observed along the rest of the SWIR, in particular West of the Melville Fracture Zone. These compositions are also in good agreement with the results of previous isotopic studies conducted in the same region (e.g. Meyzen et al., 2005; Gautheron et al., 2015). This strongly suggests that they derive from similar parent melts (Paquet et al., 2016). However, basalts erupted on ultramafic seafloor tend to be slightly more depleted for heavy radiogenic isotopes (Fig. 3) and have lower ^{4}He concentrations than those erupted at the volcanic centers (Fig. 5a). Basalts dredged off-axis show a large variability in $^{87}Sr/^{86}Sr$, which is not visible for other isotopic ratios (Figs. 2 and 4). In this section, we will discuss the mantle source composition and the effect of melt/mantle reactions on the isotopic composition of the basalts from the 61°-67°E region of the SWIR. We will also examine the across-axis variability and the evolution of the mantle source composition through time, as well as the relation between helium loss, Sr isotope compositions and seawater alteration of the oceanic crust.

5.1. Mantle source heterogeneity and effect of melt/mantle reactions on basalt isotope compositions

Samples collected on-axis during the Smoothseafloor cruise substantially refine the resolution of basalts sampled during the EDUL cruise. Spacing between dredges from both cruises ranges from 10 to up

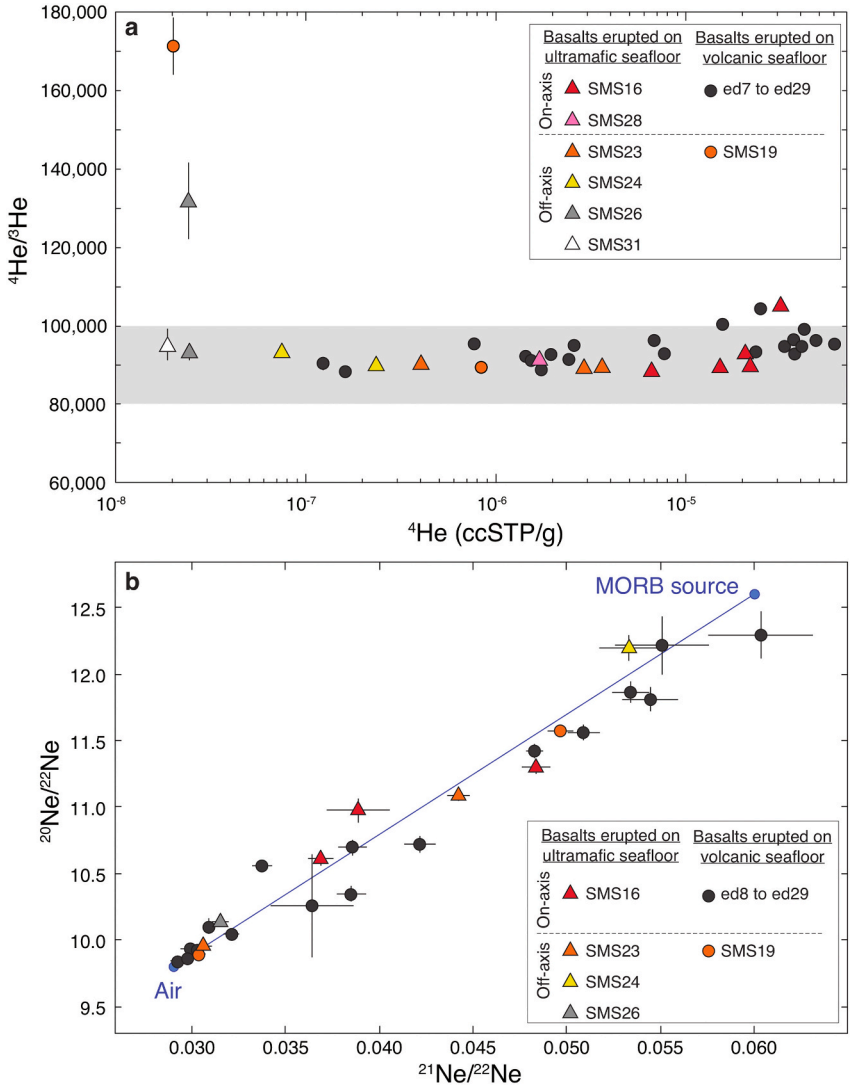

Fig. 5. (a) $^{4}He/^{3}He$ in function of ^{4}He concentration (ccSTP/g); the grey area corresponds to the mean MORB value of 90,000 ± 10,000 (Allègre et al., 1995). (b) $^{20}Ne/^{22}Ne$ in function of $^{21}Ne/^{22}Ne$. The MORB line in blue is from Sarda et al. (1988). Same symbols as in Fig. 2. (For interpretation of the references to colour in this figure legend, the reader is referred to the web version of this article.)

to 80 km (between SMS-DR16 and ED-DR16). The overall homogeneity of the isotopic and elemental compositions measured in the 61°-67°E region of the SWIR is not due to a sampling bias, with homogeneous compositions measured in basalt samples from a given dredge in most cases. This homogeneity contrasts with the isotopic variability observed along the rest of the SWIR (Figs. 2 and 6; Meyzen et al., 2003, 2005; Gautheron et al., 2015; Paquet et al., 2016). Therefore, the degree of heterogeneity along the SWIR decreases from West to East, and thus correlates with the regional decrease in crustal thickness, potential mantle temperature and increase in depth (e.g. Muller et al., 1999; Cannat et al., 1999, 2006; Meyzen et al., 2003, 2005). It is unlikely that this region experienced better homogenization of the parental melts. The very low magma supply to the ridge axis (e.g. Muller et al., 1999; Cannat et al., 1999, 2006; Sauter et al., 2013) is not expected to lead to the formation of well mixed magma bodies beneath the ridge. It is therefore likely that the mantle source is more isotopically homogeneous.

Based on major and trace element compositions, Paquet et al. (2016) showed that basalts from both types of seafloors are derived from similar parent melts, but that basalts erupted on ultramafic seafloor are more affected by reactions between these parent melts and the mantle rocks in the lithosphere below the ridge. Because on-axis basalts dredged on ultramafic seafloor display slightly less radiogenic isotope compositions in $^{206}Pb/^{204}Pb$, $^{207}Pb/^{204}Pb$, $^{208}Pb/^{204}Pb$, and $^{143}Nd/^{144}Nd$ than those erupted on volcanic seafloor (Fig. 6), we propose that melt/mantle reactions with an ambient depleted mantle could result in isotopic compositions shifted towards slightly less radiogenic values for the basalts erupted on ultramafic seafloor, relative to those from the volcanic centers (and their parent melts). Model mixtures of a Depleted MORB Mantle component (D) (from Meyzen et al., 2005) and an enriched component (E) (chosen as the composition of ED-DR11-1-1, which show the most enriched composition in the study area and could represent the parent melt isotope composition), are presented in Fig. 7. We suggest that compositions of the basalts erupted on ultramafic seafloor correspond to a contribution of the DMM of ~80% to the parent melt composition, whereas basalts erupted on volcanic seafloor are best reproduced by lower contributions of the DMM component (Fig. 7). Variations in the estimation of the enriched component would generate changes in the absolute values of the contributions of the two components to the compositions of each group of basalts, but not the general trend.

Pyroxenites were suggested as a potential mantle source contribution to explain the major element composition of the parent melts of the basalts from both types of seafloor (Paquet et al., 2016; Brunelli et al.,

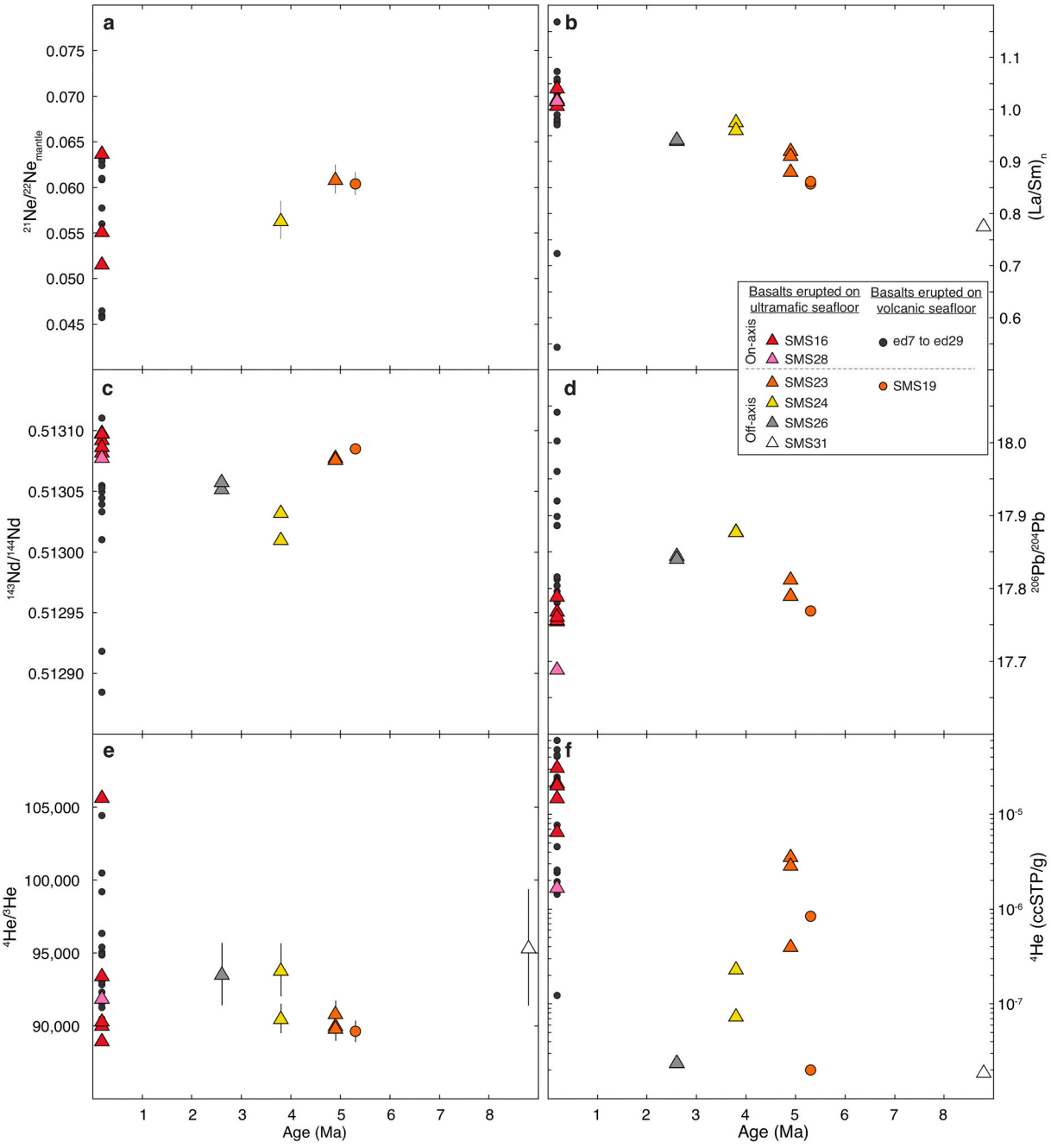

Fig. 6. (a) $^{21}Ne/^{22}Ne_{mantle}$, (b) $^{143}Nd/^{144}Nd$, (c) $^{4}He/^{3}He$, (d) $(La/Sm)_n$, (e) $^{206}Pb/^{204}Pb$, (f) ^{4}He concentration in function of the sample age. Same symbols as in Fig. 2. (For interpretation of the references to colour in this figure legend, the reader is referred to the web version of this article.)

2014, 2018). They could correspond to the slightly more enriched mantle component from which the parent melts of these lavas are derived. The easternmost SWIR is an end-member of the global ridge system in terms of its very low magma supply (Muller et al., 1999; Cannat et al., 1999, 2006) due to a lower potential mantle temperature. This would favor melting of the proposed enriched pyroxenitic component over the more refractory depleted peridotites. A heterogeneous source with several components with different solidi generates complex melting patterns depending on the degree of partial melting, homogenization and enrichment of each component (e.g. Yasuda et al., 1994; Pertermann and Hirschmann, 2003; Ito and Mahoney, 2005; Rudge et al., 2013; Shorttle, 2015). A similar process is proposed for the Vema Lithospheric Section along the Mid-Atlantic Ridge (Brunelli et al., 2018), with progressive isotopic depletion in Nd and Pb over time, suggesting a lower contribution of pyroxenite-derived melts for the younger lavas. Because basalts erupted on ultramafic and volcanic seafloors are derived from similar parent melts, we suggest that the enriched isotope compositions observed for the volcanic seafloor lavas reflect the larger contribution of pyroxenite-derived parent melts, whereas isotope compositions for the on-axis basalts erupted on ultramafic seafloor are more depleted, representing the same parent melts affected by higher degrees of melt/mantle reactions (due to lower melt/rock ratios; Paquet et al., 2016) with the ambient DMM during their ascension to the surface. Such melt/mantle reactions would also account for the slightly higher $^{3}He/^{4}He$ ratios observed for on-axis basalts dredged on ultramafic seafloor: indeed, the contribution of a pyroxenitic source has been proposed to explain lower $^{3}He/^{4}He$ isotope compositions of basalts along the SWIR (Gautheron et al., 2015) and the

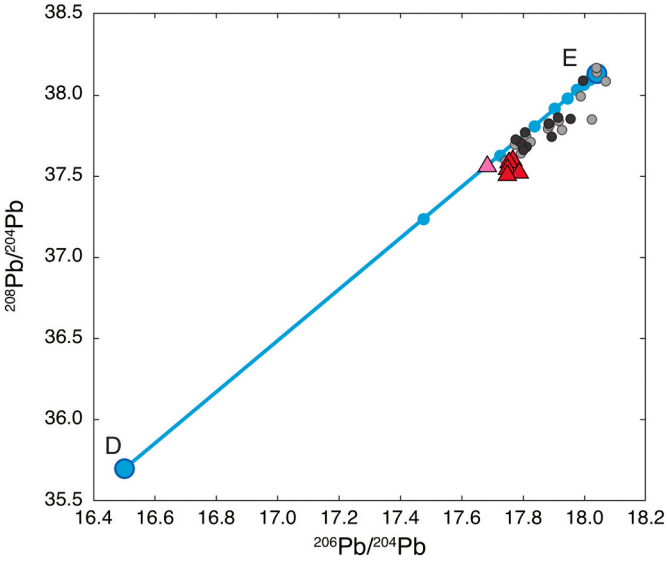

Fig. 7. Plot of $^{208}Pb/^{204}Pb$ ratios in function of $^{206}Pb/^{204}Pb$ ratios for the on-axis basalts dredged on ultramafic and volcanic seafloors from the easternmost part of the Southwest Indian Ridge, illustrating the binary mixing trajectory between a depleted component (D) and an enriched component (E). Same symbols as in Fig. 2. Dots along the mixing curve represent a 10% increment in the mixing proportions between the two endmembers. The enriched component (E) is chosen as the composition of ED-DR11-1-1, which the most enriched, and the depleted component (D) is taken as the Depleted MORB Mantle component (DMM) in Meyzen et al. (2005): Pb = 44 ppb, $^{206}Pb/^{204}Pb$ = 16.5, $^{208}Pb/^{204}Pb$ = 35.7 (see Table 3 for the model parameters). (For interpretation of the references to colour in this figure legend, the reader is referred to the web version of this article.)

SEIR (Graham et al., 2014), leading to lower $^{3}He/^{4}He$ ratios for pyroxenite-derived melts.

5.2. Helium loss, Sr isotopic composition and seawater alteration of the oceanic crust

Basalts dredged off-axis contain generally less helium than samples dredged on-axis (from 0.1 to 3.6 µccSTP/g; from 0.1 to 60 µccSTP/g, respectively) (Fig. 5a). The lower helium content observed for basalts dredged off-axis could reflect lower helium content in the mantle source at the time of their formation. However, $^{4}He/^{3}He$ ratios of basalts dredged off-axis and on-axis are similar, suggesting an isotopically homogeneous mantle source, and we note no significant correlation between $^{4}He/^{3}He$ ratios and other source indicators, such as the radiogenic isotopic ratios (Sr, Nd, Hf, Pb). Therefore, the low concentrations observed on- and off-axis lavas must result from post-melting or post-eruption processes. Another hypothesis, which we do not favor, would be that off-axis basalts did not vesiculate to the same extent during melt ascension in the axial lithosphere, due to an ascent rate too fast to allow a significant formation of vesicles. Helium would then be in the glass, not sampled with our crushing technique. However, these basalts do contain vesicles, and there is no geodynamic justification for assuming a faster ascent rate compared to on-axis basalts. A third hypothesis is that the off-axis samples have lost helium at some point before, during or after eruption. The $^{4}He/^{21}Ne^{*}$ ratio can be used as a proxy of helium loss. $^{4}He/^{21}Ne^{*}$ values in function of ^{4}He contents are represented in Fig. 8a. The data are divided in two groups. The first group, corresponding to the on-axis basalts, has $^{4}He/^{21}Ne^{*} > 2 \times 10^{7}$, which is the mantle production ratio (Yatsevich and Honda, 1997), up to 1.64×10^{8} and variable ^{4}He contents. These high $^{4}He/^{21}Ne^{*}$ values are representative of the pre-eruptive degassing (Sarda and Moreira, 2002), and the variability in He content quantifies the vesicle proportion lost during the eruption. The second group, including most of the basalts dredged off-axis, has $^{4}He/^{21}Ne^{*}$ ratios lower than 2×10^{7} with low helium content. It appears that the lower helium contents observed in the off-axis samples cannot be explained by pre-eruptive degassing and vesicle loss during the eruption.

The helium concentration in basalts dredged off-axis, dated between 2.6 and 8.8 Ma (Fig. 1), appears not correlated with the age of the lava flow (Fig. 6f). This suggests that the loss of helium occurred after the eruption. A possible explanation could be diffusion. Kurz and Jenkins (1981) determined diffusion rates for helium in basaltic glass, between 125° and 400 °C, using a stepwise heating method. The extrapolation of these results to ocean floor temperatures (0 °C) gives a diffusivity of $\sim 10^{-17}$ cm^2/s, indicating that diffusion is an insignificant mechanism for helium loss from fresh basaltic glasses. The helium diffusion distance is therefore ~0.4 mm in 5 Ma, much smaller than the size of the glassy margin (cm-scale). Thus, helium diffusion from the vesicles into the glass appears insufficient to explain the lower He contents in the basalts dredged off-axis.

The large variability in $^{87}Sr/^{86}Sr$ ratios in basalts dredged off-axis (Figs. 2b and 4b) can be interpreted as the result of seawater alteration (Alt and Teagle, 2000, and references therein), with no effect on Nd and

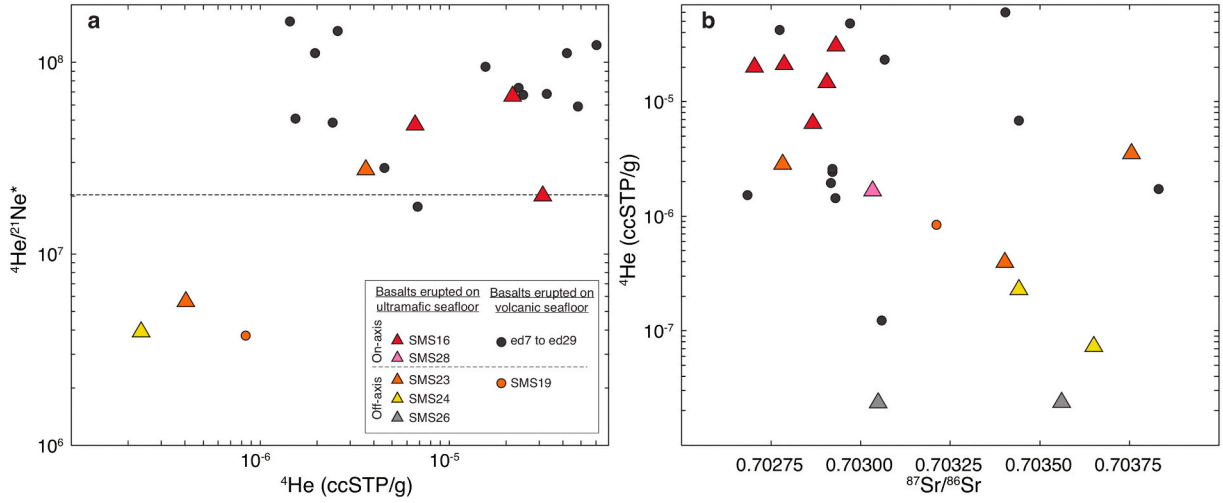

Fig. 8. (a) $^{4}He/^{21}Ne^{*}$ in function of ^{4}He concentration (ccSTP/g). The dashed line (corresponds) to the mantle reference value (Yatsevich and Honda, 1997). (b) ^{4}He concentration (ccSTP/g) in function of $^{87}Sr/^{86}Sr$. Same symbols as in Fig. 2. (For interpretation of the references to colour in this figure legend, the reader is referred to the web version of this article.)

Pb isotopic ratios. Off-axis samples with high $^{87}Sr/^{86}Sr$ ratios (associated with lower Sr contents) tend to have low ^{4}He concentration (and low ^{22}Ne concentrations, not shown) (Fig. 8b). Therefore, a possible explanation for the helium loss of the basalts dredged off-axis could simply be the alteration of the oceanic crust by seawater. Indeed, seafloor weathering is associated with the formation of cracks in the basalts, sometimes sealed by secondary minerals (e.g. Alt et al., 1986). This alteration may have opened the vesicles present in the basalts, which could explain the helium loss observed in the samples dredged off-axis.

5.3. Across-axis isotopic variability and the evolution of the mantle source composition through time

Basalt SMS-DR28-3-3 represents the present-day composition at the ridge axis of one of the sampled amagmatic corridors. The variability of the isotopic and trace element compositions of the basalts with time is investigated in Fig. 6. Because ages were estimated from their distance to the closest magnetic anomaly-based isochron, the principal source of imprecision is that, in the nearly amagmatic spreading corridors, the plate divergence is accommodated asymmetrically by large offset normal faults or detachment faults (Sauter et al., 2013; Cannat et al., 2006, 2019) that face alternately north or south and each span between 0.6 and 1.5 Ma (Cannat et al., 2019).

The variability of the $^{21}Ne/^{22}Ne_{mantle}$ does not allow us to determine a possible time-evolution of the neon isotopic signature of the mantle. However, the lavas dredged off-axis from the Southwest Indian Ridge show an increase of the $(La/Sm)_n$ ratios over the last 8.8 Ma, from 0.78 to 1.02 (Fig. 6b). Cordier et al. (2010) reported the occurrence of ancient lavas, enriched in incompatible elements, off-axis from the Central Indian Ridge (19°S). These enriched lavas are symmetrically distributed on either side of the ridge within a 40 km-long profile, representing an 800 kyr period. In their high-resolution study, these authors identified a correlation between the Sr isotope ratios and $(La/Sm)_n$ in the lavas, and interpreted the enriched melts as due to periodical variations in the aggregation processes of the melts produced from a heterogeneous mantle source. This rhythmicity in the melts collection underneath the ridge axis has been discussed in previous studies (e.g. Rabinowicz and Toplis, 2009 and references therein): they proposed that magmatic waves could be a way to maintain melts isolated from deeper region up to the base of the oceanic crust.

For the basalts dredged off-axis in the eastern corridor of the 61°-67°E region of the SWIR, the $(La/Sm)_n$ variations, observed over a longer period of time but at a lower spatial resolution, are not correlated with the $^{87}Sr/^{86}Sr$ compositions of these lavas (Fig. S1). This lack of correlation could be explained by the highly variable $^{87}Sr/^{86}Sr$ ratios reported for the lavas dredged off-axis, probably due to seawater alteration at the seafloor (see Section 5.2). The other radiogenic isotope ratios ($^{143}Nd/^{144}Nd$, $^{206}Pb/^{204}Pb$ and $^{4}He/^{3}He$) show non-linear variations with time (Fig. 6). These isotopic variations are small compared to the global variability sampled along the ridge axis for the 61°-67°E region.

Paquet et al. (2016) proposed that basalts erupted on ultramafic seafloor are more affected by melt/mantle reactions, due to lower melt/rock ratios (<60) than basalts erupted on volcanic seafloor (>100). Isotopic variations over time could reflect different melt/rock ratios during interactions of the parent melts with DMM material as they ascended through the axial lithosphere. Melt/rock ratios between 2.6 and 4.9 Ma could possibly have been higher (with a maximum at 3.8 Ma for SMS-DR24, for which the melt/rock ratio could be closer to 100) to explain the slightly enriched compositions observed for the samples dredged off-axis (compare to the present-day basalt of dredge SMS-DR28, derive from a lower melt/rock ≤60), implying a lesser effect of interactions between the parent melts of these lavas and the depleted mantle. Additionally, variations in the melt collection underneath the ridge axis through time (e.g. Rabinowicz and Toplis, 2009) could result in variations of the associated melt/rock ratio. Such variations would also be expected to correspond to a greater influx of melt to the ridge, leading to the eruption of more basalt on the seafloor between 2.6 and 4.9 Ma. Basalts would then derive from melt/rock ratios twice as high, similar to those from the volcanic seafloor. However, because accommodation of spreading in the amagmatic corridors remained mostly tectonic over the past 8.8 Ma (Sauter et al., 2013; Cannat et al., 2019), it is unlikely that variations of the melt/rock ratios over time could explain the isotopic variability observed in the basalts dredged off-axis. Even though the sampling density of the lavas dredged off-axis does not allow us to further constrain the cause of this chemical variability, it may provide a frame for future work on the effect of melt/mantle reactions on the isotopic signature of MORB with higher spatial resolution.

6. Conclusions

The eastern SWIR between 61° and 67°E has a very low melt supply and comprises several corridors of nearly amagmatic spreading that expose mantle-derived serpentinized peridotites (Cannat et al., 2003, 2006; Sauter et al., 2013). More volcanically active ridge portions separate these corridors.

- Basalts erupted on ultramafic seafloor, in particular those dredged on-axis, display slightly more depleted compositions in radiogenic isotopes than those erupted on volcanic seafloor.
- Melt/mantle reactions with an ambient depleted mantle could result in isotopic compositions slightly shifted towards less radiogenic values for the basalts erupted on ultramafic seafloor, compared to the lavas erupted at the volcanic centers.
- The temporal variability of the mantle source in an ultramafic corridor over 8.8 Ma appears to be minor compared to the overall range of isotopic variability of the on-axis lavas from the 61°-67°E region.
- Looking at these variations at broader scale, this segment of the SWIR appears largely homogeneous, compared to what is observed for the rest of this ultraslow spreading ridge.

Supplementary data to this article can be found online at https://doi.org/10.1016/j.chemgeo.2020.119741.

Declaration of competing interest

The authors declare that they have no known competing financial interests or personal relationships that could have appeared to influence the work reported in this paper.

Acknowledgments

We thank the two anonymous reviewers, and the Editor, Catherine Chauvel, for their helpful comments that helped improve the manuscript. Samples were collected the Smoothseafloor cruise (MD183) on the RV Marion Dufresne. This work was supported by the Institut National des Sciences de l'Univers (SYSTER program). Upon publication of this paper, the data will be contributed to the Petrological Database (www.earthchem.org/petdb).

References

Allègre, C.J., 1987. Isotope geodynamics. Earth Planet. Sci. Lett. 86 (2–4), 175–203.
Allègre, C.J., Moreira, M., Staudacher, T., 1995. $^{4}He/^{3}He$ dispersion and mantle convection. Geophys. Res. Lett. 22 (17), 2325–2328.
Alt, J.C., Teagle, D.A., 2000. Hydrothermal Alteration and Fluid Fluxes in Ophiolites and Oceanic Crust. Special Papers-Geological Society of America, pp. 273–282.
Alt, J.C., Honnorez, J., Laverne, C., Emmermann, R., 1986. Hydrothermal alteration of a 1 km section through the upper oceanic crust, Deep Sea Drilling Project Hole 504B: Mineralogy, chemistry and evolution of seawater-basalt interactions. Journal of Geophysical Research: Solid Earth 91 (B10), 10309–10335.

Baker, J., Peate, D., Waight, T., Meyzen, C., 2004. Pb isotopic analysis of standards and samples using a 207Pb–204Pb double spike and thallium to correct for mass bias with a double-focusing MC-ICP-MS. Chem. Geol. 211 (3–4), 275–303.
Brunelli, D., Cipriani, A., Bonatti, E., 2018. Thermal effects of pyroxenites on mantle melting below mid-ocean ridges. Nature Geoscience 11 (7), 520–525.
Brunelli, D., Paganelli, E., Seyler, M., 2014. Percolation of enriched melts during incremental open-system melting in the spinel field: A REE approach to abyssal peridotites from the Southwest Indian Ridge. Geochimica et Cosmochimica Acta 127, 190–203.
Cannat, M., Rommevaux-Jestin, C., Sauter, D., Deplus, C., Mendel, V., 1999. Formation of the axial relief at the very slow spreading Southwest Indian Ridge (49° to 69°E). Journal of Geophysical Research: Solid Earth 104 (B10), 22825–22843.
Cannat, M., Rommevaux-Jestin, C., Fujimoto, H., 2003. Melt supply variations to a magma-poor ultra-slow spreading ridge (Southwest Indian Ridge 61° to 69° E). Geochem. Geophys. Geosyst. 4 (8).
Cannat, M., Sauter, D., Mendel, V., Ruellan, E., Okino, K., Escartin, J., Combier, V., Baala, M., 2006. Modes of seafloor generation at a melt-poor ultraslow-spreading ridge. Geology 34 (7), 605–608.
Cannat, M., Sauter, D., Lavier, L., Bickert, M., Momoh, E., Leroy, S., 2019. On spreading modes and magma supply at slow and ultraslow mid-ocean ridges. Earth Planet. Sci. Lett. 519, 223–233.
Catanzaro, E.J., Murphy, T.J., Shields, W.R., Gamer, E.L., 1968. Absolute isotopie abundance ratios of common, equal-atom, and radiogenic lead isotopie standards. Notes 5, 1.
Chauvel, C., Blichert-Toft, J., 2001. A hafnium isotope and trace element perspective on melting of the depleted mantle. Earth Planet. Sci. Lett. 190 (3–4), 137–151.
Cordier, C., Benoit, M., Hémond, C., Dyment, J., Le Gall, B., Briais, A., Kitazawa, M., 2010. Time scales of melt extraction revealed by distribution of lava composition across a ridge axis. Geochem. Geophys. Geosyst. 11 (7).
Dupré, B., Allègre, C.J., 1983. Pb–Sr isotope variation in Indian Ocean basalts and mixing phenomena. Nature 303 (5913), 142.
Escrig, S., Capmas, F., Dupré, B., Allègre, C.J., 2004. Osmium isotopic constraints on the nature of the DUPAL anomaly from Indian mid-ocean-ridge basalts. Nature 431 (7004), 59.
Gautheron, C., Moreira, M., Gerin, C., Tassan-Got, L., Bezos, A., Humler, E., 2015. Constraints on the DUPAL anomaly from helium isotope systematics in the Southwest Indian mid-ocean ridge basalts. Chem. Geol. 417, 163–172.
Georgen, J.E., Kurz, M.D., Dick, H.J., Lin, J., 2003. Low ^{3}He/4He ratios in basalt glasses from the western Southwest Indian Ridge (10°-24°E). Earth Planet. Sci. Lett. 206 (3–4), 509–528.
Graham, D.W., Hanan, B.B., Hémond, C., Blichert-Toft, J., Albarède, F., 2014. Helium isotopic textures in Earth's upper mantle. Geochem. Geophys. Geosyst. 15 (5), 2048–2074.
Hamelin, B., Allègre, C.J., 1985. Large-scale regional units in the depleted upper mantle revealed by an isotope study of the Southwest Indian Ridge. Nature 315 (6016), 196.
Hamelin, B., Dupré, B., Allègre, C.J., 1986. Pb-Sr-Nd isotopic data of Indian Ocean ridges: new evidence of large-scale mapping of mantle heterogeneities. Earth Planet. Sci. Lett. 76 (3–4), 288–298.
Hamelin, C., Seitz, H.M., Barrat, J.A., Dosso, L., Maury, R.C., Chaussidon, M., 2009. A low δ^{7}Li lower crustal component: evidence from an alkalic intraplate volcanic series (Chaîne des Puys, French Massif Central). Chem. Geol. 266 (3–4), 205–217.
Hamelin, C., Bezos, A., Dosso, L., Escartin, J., Cannat, M., Mevel, C., 2013. Atypically depleted upper mantle component revealed by Hf isotopes at Lucky Strike segment. Chem. Geol. 341, 128–139.
Hanan, B.B., Blichert-Toft, J., Hemond, C., Sayit, K., Agranier, A., Graham, D.W., Albarède, F., 2013. Pb and Hf isotope variations along the Southeast Indian Ridge and the dynamic distribution of MORB source domains in the upper mantle. Earth Planet. Sci. Lett. 375, 196–208.
Hart, S.R., 1984. A large-scale isotope anomaly in the Southern Hemisphere mantle. Nature 309 (5971), 753.
Hart, S.R., 1988. Heterogeneous mantle domains: signatures, genesis and mixing chronologies. Earth Planet. Sci. Lett. 90 (3), 273–296.
Hofmann, A.W., 1997. Mantle geochemistry: the message from oceanic volcanism. Nature 385 (6613), 219.
Ito, G., Mahoney, J.J., 2005. Flow and melting of a heterogeneous mantle: 1. Method and importance to the geochemistry of ocean island and mid-ocean ridge basalts. Earth Planet. Sci. Lett. 230 (1–2), 29–46.
Janney, P.E., Le Roex, A.P., Carlson, R.W., 2005. Hafnium isotope and trace element constraints on the nature of mantle heterogeneity beneath the central Southwest Indian Ridge (13 E to 47 E). J. Petrol. 46 (12), 2427–2464.
Kurz, M.D., Jenkins, W.J., 1981. The distribution of helium in oceanic basalt glasses. Earth Planet. Sci. Lett. 53 (1), 41–54.
Le Roex, A.P., Dick, H.J., Fisher, R.L., 1989. Petrology and geochemistry of MORB from 25°E to 46°E along the Southwest Indian Ridge: evidence for contrasting styles of mantle enrichment. J. Petrol. 30 (4), 947–986.
Lehnert, K., Su, Y., Langmuir, C.H., Sarbas, B., Nohl, U., 2000. A global geochemical database structure for rocks. Geochem. Geophys. Geosyst. 1 (5).
Mahoney, J.J., Natland, J.H., White, W.M., Poreda, R., Bloomer, S.H., Fisher, R.L., Baxter, A.N., 1989. Isotopic and geochemical provinces of the western Indian Ocean spreading centers. Journal of Geophysical Research: Solid Earth 94 (B4), 4033–4052.
Mahoney, J., Le Roex, A.P., Peng, Z., Fisher, R.L., Natland, J.H., 1992. Southwestern limits of Indian Ocean Ridge Mantle and the origin of low ^{206}Pb/^{204}Pb mid-ocean ridge basalt: Isotope systematics of the central Southwest Indian Ridge (17°–50°E). Journal of Geophysical Research: Solid Earth 97 (B13), 19771–19790.
Mahoney, J.J., Graham, D.W., Christie, D.M., Johnson, K.T.M., Hall, L.S., Vonderhaar, D.L., 2002. Between a hotspot and a cold spot: isotopic variation in the Southeast Indian Ridge asthenosphere, 86°E–118°E. J. Petrol. 43 (7), 1155–1176.
Manhes, G., Minster, J.F., Allègre, C.J., 1978. Comparative uranium-thorium-lead and rubidium-strontium study of the Saint Severin amphoterite: consequences for early solar system chronology. Earth Planet. Sci. Lett. 39 (1), 14–24.
Mével, C., Agrinier, P., Cannat, M., Decitre, S., Dappoigny, A., Humler, E., Jendrzejewski, N., Kienast, J., Ludden, J., Murton, B., et al., 1997. Sampling the Southwest Indian Ridge: first results of the EDUL cruise (R/V Marion Dufresne II, August 1997). InterRidge News 6 (2), 25–26.
Meyzen, C.M., Toplis, M.J., Humler, E., Ludden, J.N., Mével, C., 2003. A discontinuity in mantle composition beneath the southwest Indian ridge. Nature 421 (6924), 731.
Meyzen, C.M., Ludden, J.N., Humler, E., Luais, B., Toplis, M.J., Mével, C., Storey, M., 2005. New insights into the origin and distribution of the DUPAL isotope anomaly in the Indian Ocean mantle from MORB of the Southwest Indian Ridge. Geochem. Geophys. Geosyst. 6 (11).
Meyzen, C.M., Blichert-Toft, J., Ludden, J.N., Humler, E., Mével, C., Albarède, F., 2007. Isotopic portrayal of the Earth's upper mantle flow field. Nature 447 (7148), 1069.
Miller, J., Miller, J.C., 2018. Statistics and Chemometrics for Analytical Chemistry, 7th edition. Pearson Education.
Moreira, M., 2013. Noble gas constraints on the origin and evolution of Earth's volatiles. Geochemical Perspectives 2 (2), 229–230.
Moreira, M., Allègre, C.J., 1998. Helium–neon systematics and the structure of the mantle. Chem. Geol. 147 (1–2), 53–59.
Moreira, M., Escartin, J., Gayer, E., Hamelin, C., Bezos, A., Guillon, F., Cannat, M., 2011. Rare gas systematics on Lucky Strike basalts (37° N, North Atlantic): evidence for efficient homogenization in a long-lived magma chamber system? Geophys. Res. Lett. 38 (8).
Muller, M.R., Minshull, T.A., White, R.S., 1999. Segmentation and melt supply at the Southwest Indian Ridge. Geology 27 (10), 867–870.
Paquet, M., Cannat, M., Brunelli, D., Hamelin, C., Humler, E., 2016. Effect of melt/mantle interactions on MORB chemistry at the easternmost Southwest Indian Ridge (61°–67°E). Geochem. Geophys. Geosyst. 17 (11), 4605–4640.
Parai, R., Mukhopadhyay, S., Standish, J.J., 2012. Heterogeneous upper mantle Ne, Ar and Xe isotopic compositions and a possible Dupal noble gas signature recorded in basalts from the Southwest Indian Ridge. Earth Planet. Sci. Lett. 359, 227–239.
Patriat, P., Segoufin, J., 1988. Reconstruction of the central Indian Ocean. Tectonophysics 155 (1–4), 211–234.
Patriat, P., Sloan, H., Sauter, D., 2008. From slow to ultraslow: a previously undetected event at the Southwest Indian Ridge at ca. 24 Ma. Geology 36 (3), 207–210.
Pertermann, M., Hirschmann, M.M., 2003. Partial melting experiments on a MORB-like pyroxenite between 2 and 3 GPa: constraints on the presence of pyroxenite in basalt source regions from solidus location and melting rate. Journal of Geophysical Research: Solid Earth 108 (B2).
Rabinowicz, M., Toplis, M.J., 2009. Melt segregation in the lower part of the partially molten mantle zone beneath an oceanic spreading centre: numerical modelling of the combined effects of shear segregation and compaction. J. Petrol. 50 (6), 1071–1106.
Raquin, A., Moreira, M., 2009. Atmospheric ^{38}Ar/^{36}Ar in the mantle: implications for the nature of the terrestrial parent bodies. Earth Planet. Sci. Lett. 287 (3–4), 551–558.
Rehkämper, M., Mezger, K., 2000. Investigation of matrix effects for Pb isotope ratio measurements by multiple collector ICP-MS: verification and application of optimized analytical protocols. J. Anal. At. Spectrom. 15 (11), 1451–1460.
Rudge, J.F., Maclennan, J., Stracke, A., 2013. The geochemical consequences of mixing melts from a heterogeneous mantle. Geochim. Cosmochim. Acta 114, 112–143.
Sarda, P., Staudacher, T., Allègre, C.J., 1988. Neon isotopes in submarine basalts. Earth Planet. Sci. Lett. 91 (1–2), 73–88.
Sarda, P., Moreira, M., Staudacher, T., Schilling, J.G., Allègre, C.J., 2000. Rare gas systematics on the southernmost Mid-Atlantic Ridge: constraints on the lower mantle and the Dupal source. Journal of Geophysical Research: Solid Earth 105 (B3), 5973–5996.
Sarda, P., Moreira, M., 2002. Vesiculation and vesicle loss in mid-ocean ridge basalt glasses: He, Ne, Ar elemental fractionation and pressure influence. eochimica et Cosmochimica Acta 66 (8), 1449–1458.
Sauter, D., Cannat, M., Rouméjon, S., Andreani, M., Birot, D., Bronner, A., Brunelli, D., Carlut, J., Delacour, A., Guyader, V., et al., 2013. Continuous exhumation of mantle-derived rocks at the Southwest Indian Ridge for 11 million years. Nat. Geosci. 6 (4), 314.
Seyler, M., Cannat, M., Mével, C., 2003. Evidence for major-element heterogeneity in the mantle source of abyssal peridotites from the Southwest Indian Ridge (52° to 68° E). Geochemistry. Geophysics, Geosystems (2), 4.
Shorttle, O., 2015. Geochemical variability in MORB controlled by concurrent mixing and crystallisation. Earth Planet. Sci. Lett. 424, 1–14.
Vervoort, J.D., Patchett, P.J., Blichert-Toft, J., Albarède, F., 1999. Relationships between Lu–Hf and Sm–Nd isotopic systems in the global sedimentary system. Earth Planet. Sci. Lett. 168 (1–2), 79–99.
Vlastelic, I., Aslanian, D., Dosso, L., Bougault, H., Olivet, J.L., Geli, L., 1999. Large-scale chemical and thermal division of the Pacific mantle. Nature 399 (6734), 345.
White, W.M., Albarède, F., Télouk, P., 2000. High-precision analysis of Pb isotope ratios by multi-collector ICP-MS. Chem. Geol. 167 (3–4), 257–270.
Yasuda, A., Fujii, T., Kurita, K., 1994. Melting phase relations of an anhydrous mid-ocean ridge basalt from 3 to 20 GPa: Implications for the behavior of subducted oceanic crust in the mantle. Journal of Geophysical Research: Solid Earth 99 (B5), 9401–9414.
Yatsevich, I., Honda, M., 1997. Production of nucleogenic neon in the Earth from natural radioactive decay. Journal of Geophysical Research: Solid Earth 102 (B5), 10291–10298.